51st AIAA Aerospace Sciences Meeting including the New Horizons Forum and Aerospace Exposition
07 - 10 January 2013, Grapevine (Dallas/Ft. Worth Region), Texas

AIAA 2013-0229

Flow Visualizations of A Simplified Linear Aerospike Model Using Background Oriented Schlieren

Hidemi Takahashi[1], Sadatake Tomioka[2], Noboru Sakuranaka[3] and Takeo Tomita[4]
Japan Aerospace Exploration Agency (JAXA), Kakuda, Miyagi, 981-1525, Japan

and

Kohei Kuwamori[5] and Goro Masuya[6]
Tohoku University, Sendai, Miyagi, 982-0858, Japan

Flow interaction between external flow and cell jet flows of a simplified clustered linear aerospike model was experimentally investigated based on the surface pressure measurements and a flow visualization using background oriented Schlieren (BOS) technique. The test model has four clustered cell nozzles with a designed Mach number of 3.47 and is connected to a straight section following a 12-degree-inclined straight ramp. It is set up in a Mach 2.0 supersonic wind tunnel to simulate conditions of supersonic external flow impinging on the cell nozzle jets and ramp surface. Under conditions with or without external flow, pressure distributions on the ramp surface were measured and compared to flow visualization results. Results of measured pressure distributions on the test model surface for the with-external flow case were obviously different due to the external flow: ramp surface pressures were maintained at a certain level above the environmental pressure level according to the cell jet expansion conditions, and the pressure distribution for conditions without-external flow can be nearly approximated by the method of characteristics. Furthermore, the external flow makes the entire flowfield on the ramp more uniform compared to that for the conditions without-external flow by eliminating periodic compression/expansion feature of jet. Flow visualization found that those tendencies are mainly governed by the fact that the external flow controls jet expansion by pressing it against the ramp wall surface. While flowfield was investigated, BOS technique itself was assessed to have better sensitivity and accuracy for a given setup.

Nomenclature

C_D = discharge coefficient
D = diameter of lens, mm
L_{cg} = length of cell gap (lateral distance between two neighboring cell nozzles), mm
L_{cze} = lateral length of cell nozzle exit, mm
M_a = freestream (external flow) Mach number
M_r = cell nozzle exhaust Mach number
NDP = Non-dimensional pressure defined as $(P-P_b)/P_{0r}$

---

[1] Researcher, Engine System Research and Development Group, Space Transportation Mission Directorate, 1 Kimigaya-Aza-Koganezawa, Kakuda, Miyagi 981-1525, Japan, Member AIAA.

[2] Senior Researcher, Advanced Technology Research Group, Space Transportation Mission Directorate, Senior Member AIAA.

[3] Associate Senior Researcher, Advanced Technology Research Group, Space Transportation Mission Directorate, Member AIAA.

[4] Senior Researcher, Engine System Research and Development Group, Space Transportation Mission Directorate, Member AIAA.

[5] Graduate Student, Department of Aerospace Engineering, Aramaki-Aza-Aoba, Aoba-ku, Sendai, Miyagi 982-0858, Japan, Student member AIAA.

[6] Professor, Department of Aerospace Engineering, Aramaki-Aza-Aoba, Aoba-ku, Sendai, Miyagi 982-0858, Japan, Senior member AIAA.

NPR	=	nozzle pressure ratio defined as P_{0r}/P_b
P_a	=	static pressure at facility nozzle exit (freestream static pressure), kPa
P_b	=	static pressure in the test chamber, kPa
P_{0a}	=	total pressure of freestream, kPa
P_{0r}	=	total pressure of cell nozzle flow, kPa
x	=	coordinate in streamwise direction, mm
y	=	coordinate in vertical direction, mm
z	=	coordinate in spanwise direction, mm
θ	=	ramp angle, deg.
σ	=	standard deviation

I. Introduction

THE TSTO (Two-Stage-to-Orbit) concept is one of the most efficient configurations for the next generation space transportation for access to orbits. The TSTO vehicle not only travels over a wide range of distances but also over a wide range of altitudes, from sea level to orbit. Therefore, its engine is exposed to various external pressure conditions. For this situation, the engine nozzle, the component which translates combustion pressure energy to thrust, needs to be capable of adjusting the optimum expansion for various altitudes so that it can maintain optimum thrust conditions for a wide operational range. Aerodynamic booms and drags of the engine must also be low in view of environmental concerns.

An aerospike nozzle or a plug nozzle is a so-called "altitude compensating nozzle," the ambient pressure of which places a limit on the expansion process of nozzle flow to adjust the area ratio associated with the ambient pressure change instead of a nozzle wall. Therefore, an aerospike nozzle yields higher thrust performance and specific impulse of various altitudes, resulting in overall higher thrust performance compared with that by conventional bell-shaped nozzles.[1-3] One of the other advantages of using an aerospike nozzle is that differential throttling[4-5] is possible by clustering the cell rockets (or nozzles) without using many small thrusters to control vehicle attitudes. By use of a clustered linear aerospike nozzle, the whole back area of a rectangular vehicle aftbody can be utilized to generate thrust. Also, it is environmentally friendly in that it causes less acoustic drag compared with use of conventional bell-shaped nozzles.[6] Therefore, a clustered linear aerospike nozzle concept provides greater advantages than conventional nozzles for an engine of a TSTO vehicle.

On the negative side, one of the biggest concerns with using an aerospike nozzle is the lack of actual flight experiences. Thus, some issues remain unclear, such as decreased performance under transonic flight conditions,[7-8] substantial thrust loss due to skin friction by the three-dimensional flow structure generated by cell bases of each clustered cell rocket nozzle, resulting in streamwise vortices generated by interaction between boundary layer and oblique shock waves running on the spike surface,[9] and necessity of detailed mechanisms of the influence of external flow on determining spike surface pressure distribution by coupling with cell nozzle flows, and also the coupling effect on the mechanism of closed/open wake[10] conditions.

Considering the thrust performance of in-flight conditions, it is particularly important to characterize the influence of external flow and its coupling effect on clustering because the external flow surrounding the vehicle aft body during flight noticeably affects the nozzle performance due to local changes of ambient pressure and resultant change in cell nozzle flow properties. To date, numerous studies have provided many insights on the influence of external flow,[11] the mechanism of closed/open wake conditions,[10] and clustering effects[12-15] in ground tests prior to flight experiments. To obtain further insights into the mechanism of the influence of external flow determining the spike surface pressures and cell base pressure behaviors, a theoretical model to predict pressure distributions has been established in our previous study[16]. It founds that the spike surface pressure under external-flow-exposed condition was mostly governed by the oblique shock wave theory with assuming certain mixing area between cell flow and external flow in one-dimensional analysis.

In order to give clearer insights and more detailed mechanism on the influence of external flow on determining the spike surface pressure distribution, flow visualization is beneficial. In this study, the background oriented Schlieren (BOS) technique, which is originally proposed by Meier[17], was employed. The BOS is a Schlieren-based flow imaging technique which measures the refraction index of light rays due to the density gradient in the flow, and thereby used as a means of visualizing the density gradient field as well as conventional Schlieren technique. One of the advantages of using BOS compared to conventional Schlieren is that the BOS is capable of deriving absolute density fields using the Gladstone-Dale relationship. While not sensitive as conventional Schlieren and necessary much time to visualize the computed density field, BOS is more amenable to quantitative analysis and to easier setup with cost effectiveness. The technique has been improved through various studies such as demonstrations of

density field measurements[18-20] and sensitivity analysis[21-22] in this decade. Still the technique highly depends on know-how for the setup, therefore further assessment to relate parameters each other toward optimizing the system for a given setup is important.

The present study focused on investigating the influence of external flow on the spike-simulated ramp surface pressure determination using the BOS technique. The goal was to identify flow interaction between cell flow and external flow and explain a mechanism how the ramp surface pressure is determined under external-flow-exposed conditions. For this reason, the BOS is mainly used to capture qualitative feature of flowfield. As a test model, a simplified straight ramp instead of a carefully designed contoured ramp was used to focus on investigating how the external flow interacts with clustered cell nozzle flows and determines the ramp surface pressure distribution. The straight ramp section is connected to the clustered cell nozzles. The Mach number of the cell nozzle was fixed at a design value of 3.47 and an external flow Mach number of 0 or 2.0. The cell nozzle flow condition was varied by changing the NPR (Nozzle Pressure Ratio), which is given as the ratio of the total pressure of the cell nozzle and environmental pressure. The cell base width and number of cell nozzles were fixed in this study. While investigating the aerodynamic performance of the clustered linear aerospike nozzles, a method to improve the sensitivity and accuracy of the BOS technique itself for a given setup was evaluated.

II. Experimental Setup and Conditions

The experimental setup and conditions for the wind tunnel experiment, and details of BOS setup are described in this section.

A. Wind Tunnel Facility

Experiments to investigate flow interactions of a simplified clustered linear aerospike nozzle model are conducted in a supersonic blowdown-type wind tunnel equipped with the Ram Jet Test Facility (RJTF) at JAXA Kakuda Space Center (KSPC). Figure 1 shows a photograph of the model setup (left) and an illustration of a front-view of the flow duct from the downstream direction (right). A two-dimensional supersonic nozzle mounted in the facility has an exit Mach number of 2.0 and the exit has a 100 mm by 100 mm square cross section (termed M2.0 facility nozzle, hereafter). Boundary layer thickness at the M2.0 facility nozzle exit is approximately 10 mm, which is measured in a separate experiment using Pitot-probe surveys. The stagnation temperature for the freestream is room temperature of about 273 K, and the stagnation pressure for the Mach 2.0 freestream is continuously varied to attain the desired conditions of static pressure. Side walls are attached on both sides of the test model to prevent the influence of undesirable three-dimensional flow on the ramp surface pressures.

The test model is directly connected to the M2.0 facility nozzle exit giving it a Mach 2.0 flow, simulating the external flow environment, but there is a small gap between the M2.0 facility nozzle exit and the test model. The 1-mm gap between them enables force measurement of the test model without additional disturbance force which could occur if the test model touched the facility. Note that, although this small gap generates some weak waves, its effect on the measured pressure is not significant and therefore key physics such as the mechanism of determining the pressure on the ramp surface is properly evaluated. The nozzle exit appears inside the test chamber where a test model is installed, and the test chamber is connected to the ejector of the facility through a diffuser to control the static pressure around the test model as an environmental pressure and to control the test conditions. The role of the extension part is to prevent expansion waves emanating from the M2.0 facility nozzle exit from impinging on the ramp surface.

B. Test Model and Clustered Cell Nozzles Characteristics

The test model was a simplified aerospike nozzle model with a set of 4 clustered cell nozzle modules and a straight ramp, as presented in Figure 2. A straight ramp was used instead of an actual contoured ramp in order to focus on the study of the influence of external flow on the pressure determination on the ramp surface. The cell nozzle exit plane was connected to the 77-mm-length straight section and the following 210-mm-length straight ramp section. The length of the straight-section was determined by the fact that the ramp section starts some distance from the cell nozzle exit where the Mach wave emanating from the cell nozzle lip (top edge of nozzle exit) interacts with the bottom surface of the straight section. The ramp angle was 12 degrees inclined against the straight section. A test model was attached to a force measurement system (TEAC MC36-250) and gaseous nitrogen (GN2) feeding lines. The cell nozzle flow was GN2. Acrylic glass windows were located on both sides of the test model as side-fences and to provide a two-dimensional Mach 2.0 flow to the ramp surface.

Cell nozzles for four-clustered (4-cell model) modules are shown in Figure 2 (a) with dimensions. The nozzle contour is in the horizontal direction, where the exit length is 22 mm and the throat width is 2.95 mm, resulting in a nozzle Mach number of 3.47. The discharge coefficient of each cell nozzle was about C_D=0.95: C_D was calculated as the ratio of static pressure measured 10 mm upstream from the cell nozzle exit and a theoretically calculated value using isentropic relations at the corresponding location. The cell nozzle height was 20 mm. Above the nozzles with a height of 20 mm, a 2.5-mm-thick plate was attached as an upper wall (shroud)[3] of the cell nozzle modules. The resultant width ratio L_{cze}/L_{cg} was 5.5 (= 22/4) for the 4-cell model. The designed NPR for the cell nozzle at the optimal-expansion condition was 73.1.

There are a total of 154 pressure ports on the surface of the straight section (totally 49 points) and the ramp section (totally 105 points), as shown in Figure 2 with red-colored dots. They are located on the grid, the interval in the x-direction of which is 10 mm and 12.5 mm in the z-direction. Also, the pressure ports are located at the base (at 3 heights on each cell base) and ramp base (totally 15 points). These wall static pressures were measured by use of an electric scanning pressure measurement system (Pressure Systems Inc. PSI ESP-64HD) at 10 Hz. Total pressure for the Mach 2.0 freestream and GN2 cell flows were measured by strain gauge pressure sensors separately but synchronized with the PSI system.

For the without-external flow case (cases of only GN2 cell nozzle flow was provided), total pressure of cell nozzle flow was maintained at a set value to provide a desired NPR. For the with-external flow case (cases of both M2.0 external flow and GN2 cell nozzle flow were provided), while cell nozzle flow total pressure was kept constant at a set value, the stagnation pressure of the M2.0 freestream was varied in a descending manner, and only when the static pressure at the M2.0 facility nozzle exit (P_a) and test chamber pressure (P_b) became equal, the data were used.

Representative experimental conditions mainly discussed in this paper are summarized in the Table 1. As mentioned the surface pressure distribution was measured using the PSI sensor system at a sampling frequency of 10 Hz. Every presented value hereafter is an averaged value for the duration of 1 second, which corresponds to 10 sampling points, when the NPR attains stability at a target condition and the error bar is a standard deviation (1σ) for the averaging duration.

Table 1 Experimental Condition for Pressure Measurements.

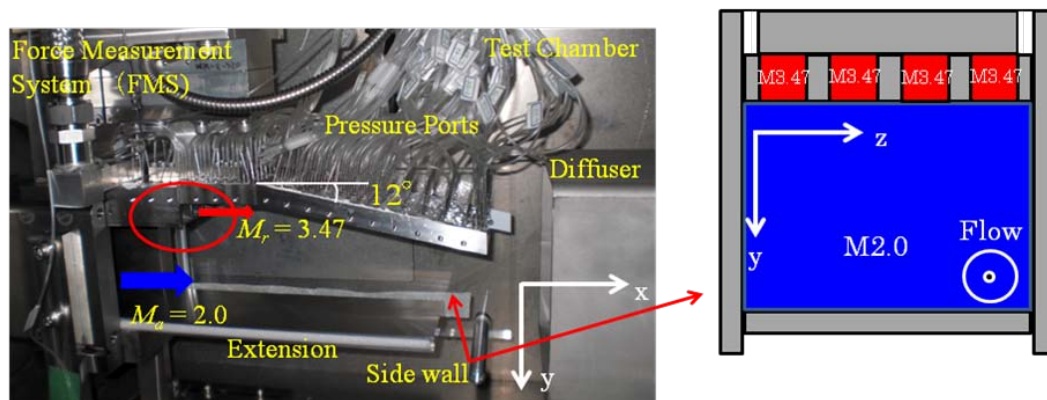| Condition of cell jet expansion	Without-external flow (cell nozzle flow only)			With-external flow		
	NPR	P_{0r}, kPa	P_b, kPa	NPR	P_{0r}, kPa	P_b, kPa
Under-expansion	**107.9** $\pm$ 0.6	896.5 $\pm$ 2.0	8.3 $\pm$ 0.03	**104.4** $\pm$ 3.4	1135.7$\pm$29.0	10.9 $\pm$ 0.1
Nearly optimal-expansion	**72.8** $\pm$ 0.3	516.8 $\pm$ 1.7	7.1 $\pm$ 0.01	**78.9** $\pm$ 1.0	991.7 $\pm$ 1.9	12.6 $\pm$ 0.1
Over-expansion	**36.1** $\pm$ 0.3	281.6 $\pm$ 1.4	7.8 $\pm$ 0.03	**43.5** $\pm$ 0.6	541.7 $\pm$ 1.5	12.5 $\pm$ 0.1

Figure 1 Photograph of experimental setup constructed in the wind tunnel facility (left). Figure on the right is an illustration of the front view of the duct from the downstream direction.

(a)   Dimensions of clustered cell nozzles with pressure port locations. A total of 49 points are used for pressure port locations on the straight section.

(b) Dimensions of ramp surface with pressure port locations. A total of 105 poitns on the ramp surface are used for pressure ports.

Figure 2 Dimensions of test model and pressure port locations for the straight and ramp sections.

C. BOS Measurement System
(a) Basic Principle of BOS

The basic concept of BOS is illustrated in Figure 3[17] and BOS setup in this study is presented in Figure 4. Key components of setup are very simple: imaging system of a CCD camera with an appropriate lens and a background pattern illuminated by a light source. This simple setup is of advantageous for imaging a flowfield and adjusting sensitivity of a given experimental setup. The principle of BOS is briefly described below. Detailed description can be found elsewhere[17]. The refractive index n and the density ρ are related through the Gladstone-Dale equation[18].

$$\frac{n-1}{\rho} = G(\lambda) \tag{1}$$

Where $G(\lambda)$ is the Gladstone-Dale constant which depends on the gas (medium) and weakly on the frequency of light used. This is assumed to be constant as same as that of the air of 0.023×10^{-3} kg/m³ in this study.

Since the deflection of a single beam of light which contains information of the spatial gradient of the refractive index integrated along the line-of-sight path, the image deflection ε is defined as:

$$\varepsilon = \frac{1}{n_0} \int_{Z_D - \Delta Z_D}^{Z_D + \Delta Z_D} \frac{\delta n}{\delta y} dz \tag{2}$$

From the geometry in Figure 3, the virtual image displacement $\triangle y'$ is related to the image displacement $\triangle y$ by the distance relationship of Z_B, Z_D, and Z_i in Figure 3 with assuming that Z_i equals to focal length f.

$$\frac{\Delta y'}{Z_B} = \frac{\Delta y}{Z_i} = \frac{\Delta y}{f} \tag{3}$$

For small deflection angles, ε can be approximated as

$$\varepsilon = \frac{\Delta y'}{Z_D} \tag{4}$$

Hence, by combining equations (3) and (4), following relationship is yielded.

$$\Delta y = \varepsilon \frac{Z_D}{Z_B} f \tag{5}$$

From above equation, sensitivity of setup is translated to the minimum detectable pixel shift of the background pattern for the given flowfield. In addition, larger focal length and Z_D/Z_B yields larger pixel displacement, and hence

5

American Institute of Aeronautics and Astronautics

smaller density gradient can be detected. However this also suggests that error inherent in the pixel displacement, such as due to the three-dimensionality of the flow or some noises, can be magnified as well. Therefore the optimum values for parameters in equation (5) have to be explored for the best sensitivity and accuracy for a given setup.
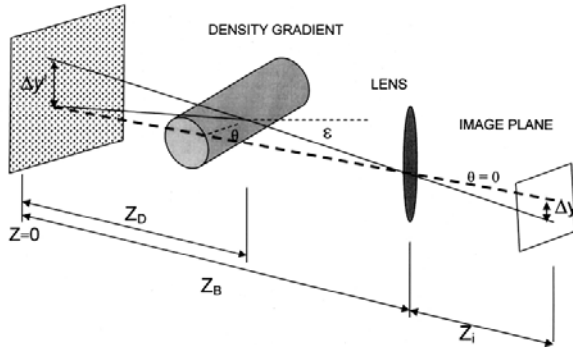

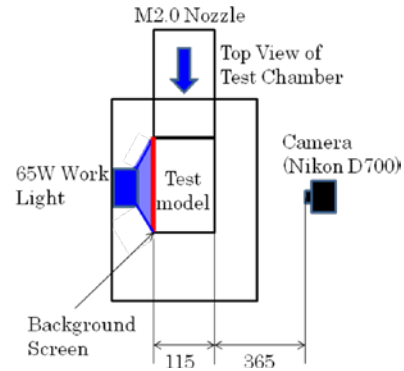**Figure 3 Schematic of BOS setup[17].**

Figure 4 BOS setup illustrated with a facility (top-view) and distance relationship for this study.

(b) BOS Setup for This Study

Table 2 summarizes parameters of BOS setup in this study. Those parameters are carefully chosen by implementing sensitivity assessment to improve accuracy and sensitivity for setup in this study.

Table 2 Parameters of BOS measurement system.

Component	Parameter	Setup in this study	Note
Camera	Shutter speed	1/50 s	Consequently acquiring only time-averaged or stable structure of flow
	Aperture (*f*-number)	F9	Background screen is in focus but the flow (media) is also nominally in focus
	ISO sensitivity	200	Minimum set value of camera used
	Spatial resolution of camera	4256 x 2832 (12M)	Allows some flexibility in locating camera lens and background screen
	Focal length (*f*)	60 mm	Determined by actual scale of test model and space limitation of facility
Background pattern	Spatial resolution of background pattern	2000 x 2000 pixels (random noise)	Background pattern is based on the random noise
	Contrast of pattern	Black and Yellow (binary)	Determined by color theory and light source used.
Overall setup	Distance between lens and density object ($Z_B - Z_D$)	365 mm	Allowing the maximum captured area.
	Distance between object and background pattern (Z_D)	115 mm	Width of test model is 100 mm and thickness of glass window is 15 mm.
Flowfield	Area of interest	Approximately 100 (H) x 250 (L)	Cell flow expansion and its interaction with external flow must be captured

Distance Relationship

Figure 4 illustrates a BOS setup and a distance relationship for this study. The background screen containing background pattern the pixel displacement of which is to be calculated was placed on the side window. As suggested by equation (5), longer distance Z_D between density gradient and background screen makes sensitivity higher, however it magnifies the error in pixel displacement as well. Therefore in order to minimize allowable error displacement, the background screen was placed on the side window where the possible Z_D becomes the minimum. At the same time, to keep certain sensitivity and considering area of interest for a photo acquisition, the distance Z_B was adjusted with given lens and camera to be 480 mm from the background screen. This distance gives the possible minimum Z_B for this setup taking into account the acquisition of area of interest and space limitations of facility.

Shutter speed, Aperture, and ISO sensitivity

Shutter speed, aperture and ISO sensitivity are closely related to each other. A shutter speed of 1/50 seconds was finally used in this study with following reason. Since Mach 3.47 flow provides a characteristic time scale of flow in the order of 1/2000 seconds by considering a flow traveling time throughout the test model, a shutter speed of 1/2000 seconds or shorter is desirable to "freeze" the flow and obtain a sharper image, especially when the flowfield is highly unstable. However once 1/2000 seconds of shutter speed is used, a captured image would be too dark and strong light source such as laser is needed to identify a pixel displacement. This eliminates an advantage in cost effectiveness and easier setup of using the BOS. Considering that the flowfield is stable, relatively longer exposure compared to a characteristic time scale of flow is allowed. In addition, it is desirable that a value of aperture which can make both background pattern and flow nominally in focus and is also desirable that a commercially available light source is used. Thus, a 1/50 seconds of shutter speed was finally determined. A resultant displacement field represents some time-averaged flow structure.

ISO sensitivity basically controls the sensitivity of sensors of camera used to a given amount of light. Higher ISO sensitivity leads to increase image noise. Therefore this value is usually set at a minimum value. This study used the minimum value of camera used and set as 200.

Aperture controls the area over which light can enter the camera lens. This is the Depth-of-Field (DOF) and important to improve sensitivity[21] of setup and to keep both the flow and background nominally in focus. DOF can be expressed as follows.

$$DOF = \frac{2d \cdot p \cdot \frac{1}{z_i}}{d^2 \cdot \left(\frac{1}{f} - \frac{1}{z_i}\right)^2 - p^2 \cdot \frac{1}{z_i^2}} \tag{6}$$

where, p a magnification factor of 0.05 mm/pixel which is determined by a captured image and unit conversion from pixel to millimeter and d the aperture. Sensitivity E in terms of DOF can be expressed as follows by combining equation (6) with some assumptions.[21,23]

$$E = \tan \varepsilon = \frac{Z_B}{Z_D} \cdot \frac{\Delta y}{Z_i}$$

$$= \frac{Z_B}{Z_D} \cdot \Delta y \cdot \frac{\left(\frac{DOF \cdot d^2}{f} + d \cdot p\right) + \sqrt{\left(\frac{DOF \cdot d^2}{f} + d \cdot p\right)^2 - \frac{DOF \cdot d^2}{f^2}\left(DOF \cdot d^2 - p^2\right)}}{DOF \cdot d^2 - p^2} \tag{7}$$

This relationship indicates that the sensitivity depends on DOF and d the aperture. A result of sensitivity analysis with given parameters described in Table 2 in case for using the minimum detectable pixel shift $\triangle y$ of 0.1 pixel is plotted in Figure 5. In this study, DOF should be greater than 115 mm because a test model has a width of 100 mm and a background screen is placed behind the 15-mm-thick side window. It is found from Figure 5 that not dramatical difference by the change of d above 16 at DOF = 115 mm is seen and below about $d = 16$ the sensitivity becomes higher. In this study, together with the shutter speed, and in order to obtain enough amount of brightness of light to identify pixel shifts, and being desired that both the background screen and flow are nominally in focus, an aperture value of 9 was finally determined.
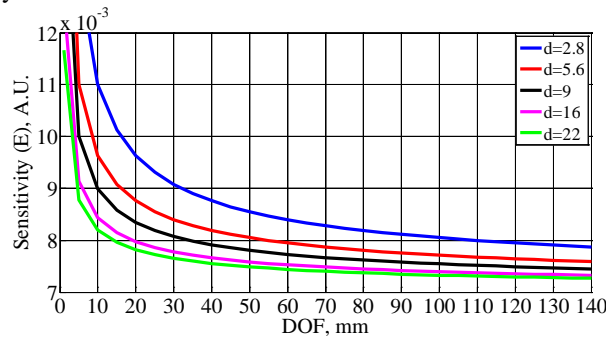

Figure 5 Sensitivity E of BOS setup based on depth of field.

7

American Institute of Aeronautics and Astronautics

Focal Length

As seen in equation (5), longer focal length is desirable to make it possible to capture smaller pixel displacement. However this can be compensated by use of a camera with higher spatial resolution. Here, a focal length of 60-mm lens was given to capture the area of interest described in Table 2 in the limited space of facility. The lens was used with a commercially available 12-megapixel class digital CCD camera (Nikon D700).

Light Source

Requirements for a light source are to be uniform and to be bright enough so that a minimum pixel displacement of interest can be identified. The brightness affects determining exposure, or shutter speed and aperture, because it determines the amount of light incoming the lens. A commercial light such as a work light or a LED array is amenable regarding cost effectiveness and easier setup if the uniformity and brightness is acceptable. In this sense, a 65-Watt class commercially available work light was used, and shutter speed and other factors are adjusted for the given brightness.

Background Pattern

Determining background pattern regarding its spatial resolution highly depends on the flow scale of interest and a diffraction limit of lens. Since an interaction between a cell jet boundary and the external flow is aimed to investigate and considering the cell nozzle exit height of 20 mm, a flow scale of interest is in the order of millimeter. The diffraction limit ε is roughly evaluated by following:

$$\varepsilon = 1.22\lambda \frac{f}{D} = 1.22 \times 780 \times 10^{-9} \times \frac{60}{62} = 920.9 \ nm \tag{8}$$

Here wavelength λ is chosen as around red color in the visible lights for example and D the lens diameter is 62 mm. This indicates that as long as spatial resolution of background pattern is greater than a micrometer range, a flow structure is possible to be resolved.

As mentioned above, a camera used here is a commercially available 12-megapixel class digital CCD camera (Nikon D700) with a 60-mm-Nikon lens. The minimum detectable dimension by the CCD sensor chip is 8.46 x 8.44 μm/pixels. Based on that a random dot pattern is used as a background pattern, if a 2000 x 2000 random dot pattern is used and printed on an A4-sized (210 x 297 mm) paper, one dot is equally spaced in every 105 x 149 μm/pixels. This dimension is larger than the diffraction limit and larger than the minimum detectable dimension by the CCD sensor, and smaller than the flow scale of interest in this study. Thus a 2000 x 2000 random dot pattern was used.

Contrast of Background Pattern

Using a color theory, a combination of black and white, or black and yellow provides higher contrast than other combinations when used for a binary random dot pattern. In this study, a binary combination of black and yellow was employed because it was found to give better contrast with regard to a light source used.

III.   Results and Discussions

Two major topics are discussed in this section: pressure distributions of the model surface and flow interactions between external flow and cell flow visualized by BOS technique.
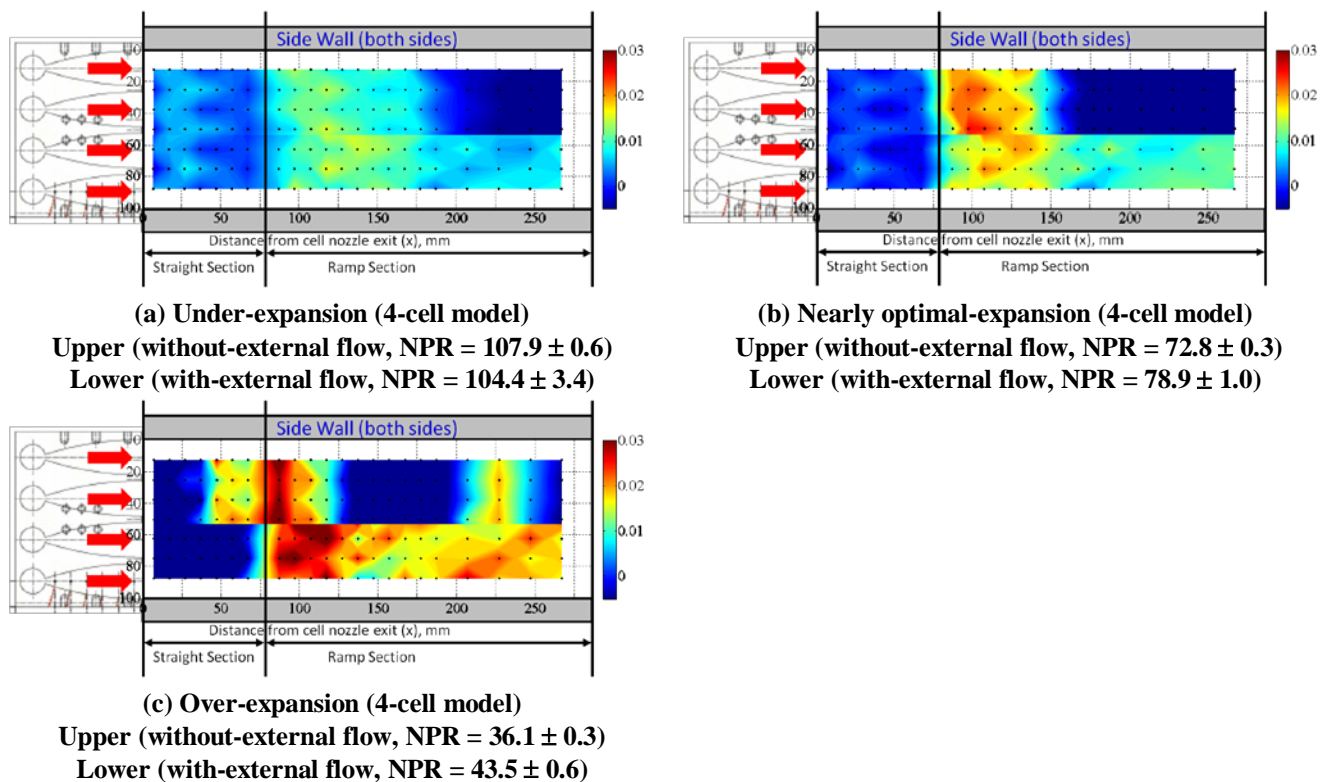
A. Surface Pressure Distributions

Surface pressure distributions for 4-cell model case are displayed in Figure 6. A non-dimensional pressure NDP defined by $(P-P_b)/P_{0r}$ is used as pressure distributions. The NDP enables pressure distributions to be evaluated equivalently by being independent of the conditional influence: P_b and P_{0r} would differ at each experimental run. Pressure port locations are superimposed as black-colored dots in each figure.

First, the flow features of all cases are compared. Figure 6 displays NDP distributions of the 4-cell model case for without- and with- external flow cases. The NDP distribution should represent flow structure near the bottom wall. Also note that the without-external flow case is given only with the GN2 cell nozzle flow. Three cases representing under-expansion (NPR $\cong$ 100), around the optimal-expansion (NPR $\cong$ 73), and over-expansion (NPR $\cong$ 38) are presented for the cases without- (upper half of figure) and with- (lower half of figure) external flow. As a general observation, flowfields are generally close to two-dimensional throughout the tested NPR range. As NPR increases and in the above optimal-expansion condition, the flow structure hardly changes except that expansion on

the ramp becomes stronger for higher NPR. However, flow structure changes are prominent in the over-expansion range by shock cell formation. It is evident that the compression region moves upward as NPR decreases. This is because the entire flowfield is more like two-dimensional flow due to this narrow cell base width (interval between neighboring two cell nozzles), and hence neighboring cell flows appear to combine, resulting in the flow structure becoming more like two-dimensional. As seen in our previous study,[16] the three peculiar high-pressure spots seen in the wider-cell base width model are not seen, but the compression region right behind the ramp corner spreads widely in the spanwise direction.

 Summarizing the flow features, the 4-cell model with a relatively narrower cell base width produces a more two-dimensional structure. For the NPR range above the optimal-expansion condition, whether with- or without-external flow, has little influence up to $x = 150$ mm. Then the flow expands further to below the environmental pressure level for the case without-external flow and flow is maintained at a certain pressure value for the case with-external flow. In view of the thrust generated by ramp pressures, the external flow aids thrust since it results in maintenance of the ramp pressure at a higher level than the environment pressure level. With decreasing NPR, the spanwise compression region moves upward and this is more prominent in the over-expansion range. Plus, in the over-expansion range, shock cell formation is evident. Over the NPR range greater than the optimal-expansion condition, the flow structure hardly changes. It should be noted that the pressures on the straight section for over-expansion conditions are strongly affected by the external flow. This might be because of the incident virtually and locally accelerated external flow at the shroud lip to bottom surface.


(a) Under-expansion (4-cell model)
Upper (without-external flow, NPR = 107.9 ± 0.6)
Lower (with-external flow, NPR = 104.4 ± 3.4)

(b) Nearly optimal-expansion (4-cell model)
Upper (without-external flow, NPR = 72.8 ± 0.3)
Lower (with-external flow, NPR = 78.9 ± 1.0)

(c) Over-expansion (4-cell model)
Upper (without-external flow, NPR = 36.1 ± 0.3)
Lower (with-external flow, NPR = 43.5 ± 0.6)

Figure 6 Surface pressure distributions on straight and ramp sections for 4-cell model case. Flow direction is from left to right.

B. Flow Visualization by BOS

 Representative results of BOS flow visualization are given in this section to compare the difference in flow structure between without- and with-external flow cases. Only an over-expansion condition case (NPR = 34.1 for without-external flow case and 37.5 for with-external flow case) is presented here. Figure 7 presents a pair of two types of raw images collected during a single experimental run for a case without-external flow at an over-expansion condition: (a) reference image with no flow (background image); and (b) one representative single-shot image with flows (experimental image). The background image is used as a reference image from which the pixel displacement corresponding to the density gradient is to be calculated. Those images were saved in a disk as a JPEG format with

9
American Institute of Aeronautics and Astronautics

8-bit pixel depth. The displayed images contain cell nozzle exit (top left side of the image), straight section (same horizontal line as the top of the image) which ends at around x = 1500 pixels, and ramp section. Flow direction is from left to right. Note that, since the commercially available non-calibrated work light was used, the brightness of illumination is not uniform: the right end is darker than other region in the image. In addition, though there are some cracks on the images, as long as they stay at the same place they do not lead significant error for identifying pixel displacements. The experimental condition and parameters for BOS setup are summarized in Tables 1 and 2, respectively. Sensitivity assessment mentioned before indicates this system has enough spatial resolution and sensitivity to visualize flow structure formed by interaction by jets, shock waves and external flow which are flow structure of interest in this study.
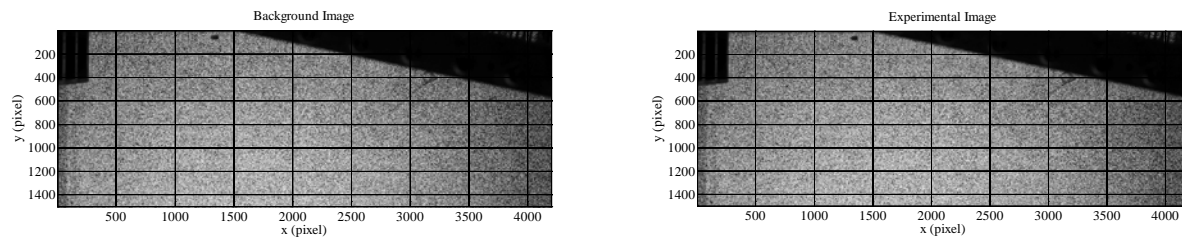
(a) Reference (background) image with no flow.   **(b) Experimental image with flows.**
Figure 7 A pair of raw single-shot images: (a) reference (w/o flow); and (b) experimental (w/ flow). This is a case without-external flow at an over-expansion condition. Flow is from left to right.

Throughout the experiments, both the background pattern and the test model were nominally in focus. An experimental image is correlated with the background image with the instantaneous displacement of the background dots. Only a single-pair of those two kinds of images were used. To correlate those two images and then identify the displaced pixel movement, the minimum quadric differences (MQD) algorithm was employed. This is because of that the MQD method is more suitable for correlating the static background displacements than using a correlation algorithm. Geometrical distortions between two images due to starting-up process of wind tunnel were corrected prior to the correlation processing. The interrogation window size was 16 x 16 pixels resultant recursive steps of 3 starting from 64 x 64 pixels with overlap of 50%. This interrogation window size was found to be providing the least error displacements. Therefore a spatial resolution is limited by the interrogation window size of 16 x 16 pixels out of the full image size of 4200 x 1500 pixels.

Figure 8 displays the post-processed pixel displacement fields in: (a) x-direction; and (b) y-direction generated from one representative single-shot image pair during a test run for a case of without-external flow at an over-expansion condition. Wall surface is highlighted by the white-colored line. Color bar represents the pixel displacement. For the displacement in x-direction, a positive value represents the region where the density gradient occurs toward downstream direction and a negative value the upstream direction. For the displacement in y-direction, a positive value represents the region where the density gradient occurs outward from the wall and a negative value toward the wall. Some error vectors and noises are still seen in the post-processed results though the allowable error level had been adjusted to be the minimum. Not to shown here but by correlating two background images with no-flow condition, the maximum error pixel displacement caused by light non-uniformity and other background noises were found to be up to 0.1 pixels in displacement. Note that the BOS visualization provides only the line-of-sight integrated density gradient information. Therefore a calculated displacement field indicates a line-of-sight integrated flow structure. Since the surface pressure distribution presented in Figure 6 indicates that the flowfield might be almost two-dimensional though the test model is clustered with 4 cell nozzles, resulting displacement fields can be regard as almost two-dimensional flow structure. From Figure 8 (a) and (b), clearly the displacement in the y-direction is evident compared to that in the x-direction. For the without-external flow case in the x-direction, only an initial part of the oblique shock wave emanating from the ramp corner (entrance of the ramp) is evident. On the contrary flow structure is clearly seen in the y-direction such as an oblique shock wave emanating from the cell nozzle lip (presented in the blue region on the straight section), jet boundary, an oblique shock wave emanating from the ramp corner and its interaction with jet boundary (strong red region just behind the ramp corner), and expansion/compression process of jet on the ramp surface. The weak displacement of jet boundary on the ramp might indicate that the jet itself expands further on the ramp surface in this area of interest. Considering the direction of density gradient, most of the jet expansion direction dominates in the y-direction. Boundary layer thickness is approximately 5 mm throughout the flowfield, and hence most of the jet core remains until at least the half length of the entire ramp, the area of interest.

10
American Institute of Aeronautics and Astronautics

Figure 9 displays the post-processed pixel displacement fields for the with-external flow case in the same manner as Figure 8. Note that the background image was chosen from an image only the external flow exists and the experimental image was chosen from an image which contains both external flow and cell jet flows in order to investigate the interaction between external flow and cell jet flows. Therefore the resultant displacement field represents region where an interaction between external flow and jet flow dominates. Clearly more complicated flow structure and interactions between shock waves and jet boundary are seen. Remarkable differences compared to the without-external flow case are seen due to the existence of external flow. A double oblique shock wave from the ramp corner is evident in the displacement in x-direction. This is because of two different flows with different velocities compressed at the ramp corner. An expansion fan emanating from the cell nozzle lip is evident in the displacement in y-direction. The most remarkable difference from the without-external flow case is in that the strong jet boundary exists along the ramp wall almost parallel to the wall surface. This is due to a slip surface between two flows with different velocities. Therefore in this slip surface since two flows have different velocity two flows mix by involving small scale vortices, and hence the thickness of this slip surface becomes thicker as it goes downstream. The thickness spans around 10 mm or approximately half the jet exit width. This is not seen in the without-external flow case. Therefore one can say that the influence of external flow appears as that the external flow controls jet expansion by pressing jet boundary against the wall and makes the jet stay on the ramp surface. As another features of influence of external flow, as discussed in Ref. 16, it is seen that due to locally decreased static pressure around the cell nozzle top edge because of Prandtl-Meyer expansion, the jet boundary expands more outwards compared to the case without-external flow. This feature is seen by comparing the displacement field in y-direction between for without- and with-external flow cases.

Together with the pressure distribution in Figure 6, those discussions make sense that the jet expands on the ramp surface because of the expansion/compression process of the jet for without-external flow case. Imaged region corresponds to the expansion region and this consistent with the observation that the wall surface pressure decreased below the environmental pressure level in this region. For the with-external flow case, due to the existence of external flow, the jet boundary is pressed against the wall surface, and consequently the jet boundary does not expand outward and stays on the wall instead. It seems this is a main mechanism of that the wall surface pressure for the with-external flow case has some certain value above the environmental pressure level. Thus the external flow influences the cell jet behavior and dominates the pressure determination process on the ramp surface.
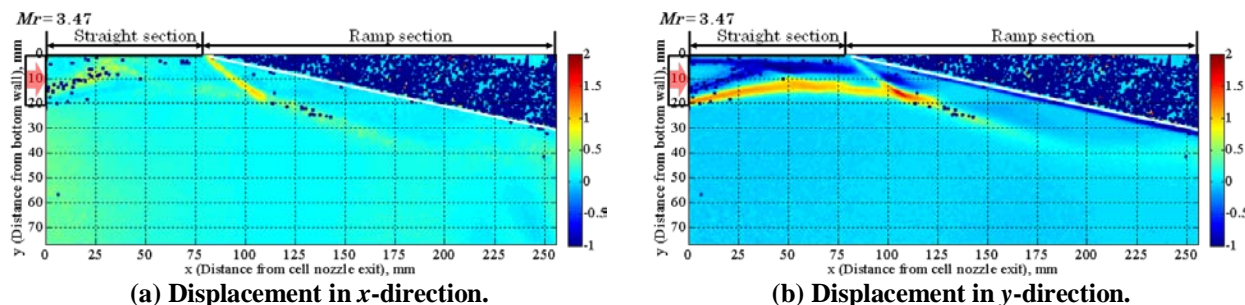

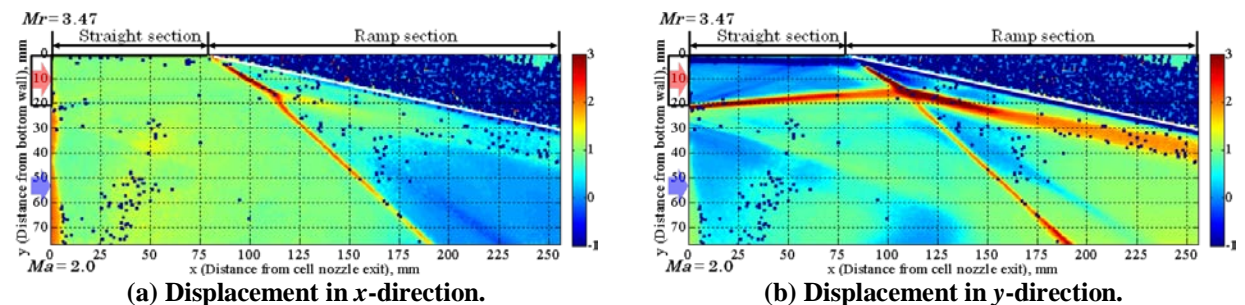| (a) Displacement in x-direction. | (b) Displacement in y-direction. |

Figure 8 Post-processed pixel displacements in x-direction (a) and y-direction (b) for a without-external flow case at an over-expansion condition (NPR = 34.1 ± 0.1). Flow is from left to right.

| (a) Displacement in x-direction. | (b) Displacement in y-direction. |

Figure 9 Post-processed pixel displacements in x-direction (a) and y-direction (b) for a with-external flow case at an over-expansion condition (NPR = 37.5 ± 0.2). Flow is from left to right.

IV. Summary

An influence of external flow on determining the ramp surface pressure distribution of a clustered linear aerospike model was investigated based on wall surface pressure measurements and BOS flow visualization. Some characteristics of the influence of external flow on the ramp pressure determination mechanism were revealed as follows:

1) Jet expansion process and most of flow structure are dominated in the vertical direction to flow direction.
2) For the without-external flow case at an over-expansion condition, interaction between jet boundary and oblique shock wave generated from the ramp corner makes strong density gradients, and the density gradient around the jet boundary gradually diminishes as it goes downstream due to expansion of jet in the tested area. This behavior consistent with the observation in the wall surface pressure measurement and explains the periodic compression/expansion feature of pressure distribution.
3) For the with-external flow case at an over-expansion condition, remarkable differences in flow structure are seen. The most remarkable difference is that the jet boundary due to a slip surface between jet and external flow stays along the ramp wall surface because the external flow presses the jet boundary against the wall. This explains the mechanism how the ramp surface pressure maintains at a certain value above the environmental pressure level.
4) External flow tends to eliminate highly periodic compression/expansion features of jet as well.

For further study, different NPR range will be investigated with the BOS technique regarding the flow structure and quantitative analysis in density fields. And a true two-dimensional cell nozzle will be employed for wall surface pressure measurement and flow visualization. Also, a carefully designed contoured ramp will be used.

Acknowledgments

References

[1]Gross, K. W., "Performance Analysis of Aerospike Rocket Engines," nasa_techdoc_19730004121, Aug. 1972.

[2]Korte, J. J., Salas, A. O., Dunn, H. J., and Alexandrov, N. M., "Multidisciplinary Approach to Linear Aerospike Nozzle Optimization," AIAA Paper 1997-3374, 1997.

[3]Onofri, M., "Plug Nozzles: Summary of Flow Features and Engine Performance," AIAA Paper 2002-0584, 2002.

[4]Hall, C., and Panossian, H., "X-33 Attitude Control Using the XRS-2200 Linear Aerospike Engine," AIAA Paper 1999-2936, 1999.

[5]Shannon, D. E., Matthew, D. W., Stephan, A. W., and Zachary, W. P., "Side-Force Amplification on an Aerodynamically Thrust-Vectored Aerospike Nozzle," *Journal of Propulsion and Power*, Vol. 28, No. 4, July 2012, pp. 811-819.

[6]Das, I. S., and Dosanjh, D.S., "Short Conical Solid/Perforated Plug-Nozzle as Supersonic Jet Noise Suppressor," *Journal of Sound and Vibration*, Vol. 146, No. 3, 1991, pp. 391-406.

[7]Ruf, J., and McConaughey, P. K., "The Plume Physics Behind Aerospike Nozzle Altitude Compensation and Slipstream Effect," AIAA Paper 1997-3218, 1997.

[8]Miyamoto, H. and Matsuo, A., "Numerical Analysis of Rectangular Plug Nozzle Considering Practical Geometry and Flow Conditions," AIAA Paper 2007-31, 2007.

[9]Goyne, C. P., Stalker, R. J., and Paull, A., "Shock-Tunnel Skin-Friction Measurements in a Supersonic Combustor," *Journal of Propulsion and Power*, Vol. 15, No. 5, 1999, pp.699-705.

[10]Geron, M., Paciorri, R., Nasuti, F., Sabetta, F., and Martelli, E., "Transition between Open and Closed Wake in 3D Linear Aerospike Nozzles," AIAA Paper 2005-4308, 2005.

[11]Bannink, W. J., Houtman, E. M., Schoones, M. M. J., "On the Interaction between a Linear Plug Nozzle Exhaust Flow and Supersonic External Flow," Proceedings of the Third European Symposium on Aerothermodynamics for Space Vehicles, ESA SP-426, Dec. 1998.

[12]Fick, M., and Schmucker, R. H., "Performance Aspects of Plug Cluster Nozzles," *Journal of Spacecraft and Rockets*, Vol. 33, No. 4, July 1996, pp. 507-512.

[13]Tsutsumi, S., Yamaguchi, K., Teramoto, S., and Nagashima, T., "Clustering Effects on Performance and Heating of a Linear Aerospike Nozzle," AIAA Paper 2007-122, 2007.

[14]Tomita, T., Takahashi, M., Tamura, H., "Flow Field of Clustered Plug Nozzles," AIAA Paper 1997-3219, 1997.

[15]Tomita, T., Takahashi, M., Onodera, T., and Tamura, H., "A Simple Performance Prediction Model of Clustered Linear Aerospike Nozzles," AIAA Paper 2001-3560, 2001.

[16]Takahashi, H., Tomioka, S., Sakuranaka, N., Tomita, T., Kuwamori, K., and Masuya, G., "Experimental Study on the Aerodynamic Performance of Clustered Linear Aerospike Nozzles," AIAA Paper 2012-5933, 2012.

[17]Meier, G., "New Optical Tools for Fluid Mechanics," Proceedings of 8th International Symposium of Flow Visualization, 1999.

[18]Venkatakrishnan, L., and Meier, G. E. A., "Density Measurements Using the Background Oriented Schlieren Technique," *Experiments in Fluids*, Vol. 37, pp. 237-247, 2004.

[19]Klinge, F., Kirmse, T., and Kompenhans, J., "Application of Quantitative Background Oriented Schlieren (BOS): Investigation of a Wing Tip Vortex in a Transonic Wind Tunnel," Proceedings of PSFVIP-4, 2003.

[20]Clem, M., Zaman, K., and Fagan, A., "Background Oriented Schlieren Applied to Study Shock Spacing in a Screeching Circular Jet," AIAA Paper 2012-0403, 2012.

[21]Bichal, A., and Thurow, B., "Development of a Background Oriented Schlieren Based Wavefront Sensor for Aero-Optics," AIAA Paper 2010-4842, 2010.

[22]Goldhahn, E., and Seume, J., "The Backgdound Oriented Schlieren Technique: Sensitivity, Accuracy, Resolution and Application to a Three-Dimensional Density Field," *Experiments in Fluids*, Vol. 43, No. 2-3, pp. 241-249, 2007.

[23]Kingslake, R., *Optics in Photography*, SPIE Optical Engineering Press, Bellingham, Washington, USA, 1992, Chap. 5, pp. 84-88.